JOURNAL OF SPACECRAFT AND ROCKETS
Vol. 59, No. 5, September–October 2022

Focused Laser Differential Interferometric Investigation of Turbulent Jet Spectra

Ahsan Hameed* and Nick J. Parziale†
Stevens Institute of Technology, Hoboken, New Jersey 07030

https://doi.org/10.2514/1.A35292

In this work, a model of focused laser differential interferometry (FLDI) is derived by incorporating the local intensity of each beam in an FLDI beam pair. We rederive some known transfer functions to reduce FLDI data. Additional transfer functions are also derived, intended to model increasingly complex disturbance fields, namely, isotropic turbulence. The new transfer functions account for disturbances not only in the streamwise direction but also in the two spanwise directions. Additionally, it is shown that strategically selecting the integration limits for the idealized FLDI in the denominator of the transfer functions ($\mathrm{d}\phi/\mathrm{d}x$) can simplify the FLDI data-reduction procedure. This is done for disturbance fields in a finite boundary (e.g., a wind tunnel of scale $\pm L$), by removing the need to characterize the FLDI probe-volume length scale. Finally, results are presented from experiments performed with a turbulent jet probed by an FLDI that indicate that increasing the complexity of the transfer function has merit with some qualifications.

Nomenclature

c_p	=	phase speed, m/s
$E_{11\rho}$	=	energy spectra of density fluctuations, $\mathrm{m(kg/m^3)^2}$
f	=	frequency, Hz
$I(x, y, z)$	=	intensity of beam along its propagation axis, $\mathrm{W/m^2}$
I_D	=	intensity at the detector face, $\mathrm{W/m^2}$
K	=	Gladstone–Dale constant
L	=	length scale, m
L_p	=	characteristic length of the focused laser differential interferometry probe volume, m
$n(x, y, z)$	=	index of refraction of the flowfield
OPL	=	optical path length, m
$R_{11\rho}$	=	autocorrelation function
V_D	=	voltage response of photodetector, V
$w(z)$	=	$1/e^2$ radius of beam varying along its propagation axis, m
w_0	=	beam waist radius at the point of best focus, m
z_0	=	location of jet, m
Δx	=	beam spacing, m
$\Delta\phi$	=	phase change
η	=	Kolmogorov length scale, m
κ	=	wavenumber, 1/m
λ	=	wavelength of the laser, m
ρ	=	local density, $\mathrm{kg/m^3}$
σ	=	width of jet at measurement point, m

I. Introduction

FOCUSED laser differential interferometry (FLDI) is a non-particle-based, optical diagnostic technique pioneered by Smeets and George [1–7] in the 1970s. Smeets and George demonstrated the use of FLDI for measurements of a density profile within a shock front and unsteady boundary layers, and, amongst other things, developed an eight-beam-pair FLDI setup to examine the flowfield around a blunt cone. From the 1970s to the 2000s, other researchers have used laser differential interferometry (LDI) to make measurements in high-speed flows [8–17]. In the early 2010s, Parziale et al. [18–24] used the FLDI technique to characterize facility disturbance level and boundary-layer instability and transition in the Caltech T5 reflected-shock tunnel. More recently, researchers from several groups have made additional advancements, including making reliable convective velocity measurements between two closely spaced FLDI probe volumes [25–34], facility disturbance-level characterization [35–37], rigor in design [38], and novel beam shaping techniques for application in hard-to-access flows [39–47].

Quantitative density-fluctuation data may be obtained by applying data-reduction strategies to raw FLDI signals. The most popular of these strategies is to transform the FLDI data into frequency space and apply so-called "transfer functions" that account for geometric optics and the characteristics of the probed disturbance field [48–50]. Parziale et al. [23] considered the differencing nature of the FLDI instrument to correct freestream disturbance spectra. Since then, data-reduction strategies by Fulghum [48], Settles and Fulghum [49], and Schmidt and Shepherd [50] have been applied to jet experiments to account for geometric optics as well as the differencing nature of the FLDI instrument. Ceruzzi et al. [27–29] have furthered these efforts and applied these transfer functions to assess the noise level in high-speed facilities. Finally, this strategy of transforming FLDI data to frequency space and applying transfer functions has been tested and evaluated by using controlled problems devised by researchers [51–55].

In this paper, a derivation of the FLDI response is proposed that accounts for the variation of intensity of the beam profile in the phase-change relation. A methodology for developing new transfer functions for the FLDI instrument is proposed, and its fidelity is tested by reproducing transfer functions familiar in the FLDI literature. This process is then used to produce new transfer functions for more general disturbance fields, namely, isotropic turbulence. Finally, these transfer functions are applied to the measured FLDI response as the instrument probes a turbulent jet flow.

II. Model of the FLDI and Relation to Voltage Output

In an FLDI system, two beams traverse closely spaced paths (in this case, the z direction; see Fig. 1), are mixed with a polarization optic, and are then registered at a photodetector. The voltage response from the photodetector, V_D, is the integrated intensity over the sensor face:

$$V_D = \bar{I}_D R_S R_L = R_S R_L \int_{A_S} I_D(x, y)\,\mathrm{d}A \tag{1}$$

where $I_D(x, y)$, $\bar{I}_D$, R_S, R_L, and A_S are the intensity at the detector face, integrated intensity, the responsivity of the photodetector, the load resistance, and the sensor area, respectively. At the photodetector face,

Presented as Paper 2021-2907 at the AIAA Aviation 2021 Forum, Virtual Event, August 2–6, 2021; received 26 October 2021; revision received 29 March 2022; accepted for publication 11 May 2022; published online 8 June 2022.

*Graduate Student, Mechanical Engineering, Castle Point on Hudson.
†Associate Professor, Mechanical Engineering, Castle Point on Hudson.

the intensity of the optical signal generated by the FLDI beams can be related to the phase change as

$$\bar{I}_D = \bar{I}_1 + \bar{I}_2 + 2\sqrt{\bar{I}_1 \bar{I}_2}\cos(\Delta\phi) \tag{2}$$

where $\bar{I}_1$ and $\bar{I}_2$ are the integrated intensity of each FLDI beam. Assuming $\bar{I}_1 = \bar{I}_2 = \bar{I}_0/2$, where $\bar{I}_0$ is the initial intensity of the beam at the outlet of the laser, and shifting the instrument by $\pi/2$ to the middle of a fringe, Eq. (2) reduces to

$$\bar{I}_D = \bar{I}_0 + \bar{I}_0 \sin(\Delta\phi) \tag{3}$$

Following Eq. (1), the voltage measured by the photodetector when the instrument is at the middle of a fringe is $V_0 = \bar{I}_0 R_S R_L$. Equation (3) can then be rewritten to relate the voltage response to the phase change as

$$\Delta\phi = \sin^{-1}\left(\frac{V_D - V_0}{V_0}\right) \tag{4}$$

Having related the voltage and phase change, the aim is now to relate density disturbance to phase change. As a density disturbance field passes through the FLDI beams, these closely spaced beams traverse different optical path lengths (OPLs). This difference in OPLs results in a phase difference between the beams of the FLDI instrument, which is expressed as

$$\Delta\phi = \frac{2\pi}{\lambda}(\mathrm{OPL}_1 - \mathrm{OPL}_2) = \frac{2\pi}{\lambda}\left(\int_{s_1} n(x,y,z)\,\mathrm{d}z - \int_{s_2} n(x,y,z)\,\mathrm{d}z\right) \tag{5}$$

where $n(x, y, z)$ is the index of refraction of the flowfield, λ is the wavelength of the laser, and s_1 and s_2 are the paths of the two FLDI beams. However, in practice, the voltage change measured by the photodetector is also dependent on the local intensity. For an FLDI instrument, this means that changes in index of refraction that occur at higher levels of intensity contribute more to the phase difference measured by the photodetector, and so the spatial distribution of intensity must be accounted for. As in Fig. 1, each FLDI beam is displaced from the origin along the ordinate by half the beam spacing, Δx, as $I[x \pm (\Delta x/2), y, z]$. Mathematically, the change in phase is modified by introducing the local intensity of each beam into Eq. (5) via multiplication by $A_1 = A_2 = 1$ as

$$\Delta\phi = \frac{2\pi}{\lambda}\left[A_1 \int_{s_1} n(x,y,z)\,\mathrm{d}z - A_2 \int_{s_2} n(x,y,z)\,\mathrm{d}z\right] \tag{6}$$

where

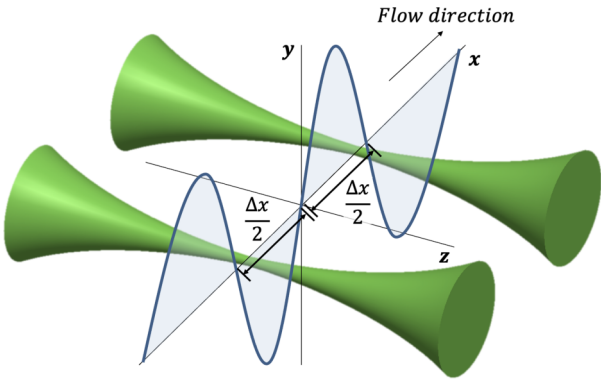

Fig. 1 Representation of FLDI beam pairs at spatial origin.

$$A_1 = \left(\frac{\iint_{-\infty}^{\infty} I(x - \frac{\Delta x}{2}, y, z)\,\mathrm{d}x\,\mathrm{d}y}{\iint_{-\infty}^{\infty} I(x - \frac{\Delta x}{2}, y, z)\,\mathrm{d}x\,\mathrm{d}y}\right)$$

$$A_2 = \left(\frac{\iint_{-\infty}^{\infty} I(x + \frac{\Delta x}{2}, y, z)\,\mathrm{d}x\,\mathrm{d}y}{\iint_{-\infty}^{\infty} I(x + \frac{\Delta x}{2}, y, z)\,\mathrm{d}x\,\mathrm{d}y}\right)$$

To model the beam intensity, we assume a Gaussian beam profile given by

$$I(x,y,z) = \frac{2}{w(z)^2\pi}\exp\left[\frac{-2(x^2+y^2)}{w(z)^2}\right] \tag{7}$$

where $w(z)$ is the $1/e^2$ radius of the beam varying along its propagation axis, z, and is given by

$$w(z) = \sqrt{w_0^2\left(1 + \left[\frac{\lambda z}{\pi w_0^2}\right]^2\right)} \tag{8}$$

where w_0 is the beam waist radius at the point of best focus. For a Gaussian beam, $\iint_{-\infty}^{\infty} I(x \pm \Delta x/2, y, z)\,\mathrm{d}x\,\mathrm{d}y = 1$ for any z. Additionally, it is assumed that the integration bounds in z are equal as $s_1 = s_2 = s$. With these assumptions, Eq. (6) is rewritten by bringing the local intensity into each line integral as

$$\Delta\phi = \frac{2\pi}{\lambda}\left[\iint_{-\infty}^{\infty}\int_s I\left(x - \frac{\Delta x}{2}, y, z\right) n(x,y,z)\,\mathrm{d}z\,\mathrm{d}x\,\mathrm{d}y - \iint_{-\infty}^{\infty}\int_s I\left(x + \frac{\Delta x}{2}, y, z\right) n(x,y,z)\,\mathrm{d}z\,\mathrm{d}x\,\mathrm{d}y\right] \tag{9}$$

Next, the Gladstone–Dale relation, $n = K\rho + 1$, is used to relate the local index of refraction to the local density. Here, K is the Gladstone–Dale constant and ρ is the local density. Inserting the Gladstone–Dale relation into Eq. (9) and dividing by the beam spacing yields

$$\begin{aligned}\frac{\Delta\phi}{\Delta x} &= \frac{2\pi K}{\Delta x\lambda}\left[\iint_{-\infty}^{\infty}\int_s I\left(x - \frac{\Delta x}{2}, y, z\right)\rho(x,y,z)\,\mathrm{d}z\,\mathrm{d}x\,\mathrm{d}y - \iint_{-\infty}^{\infty}\int_s I\left(x + \frac{\Delta x}{2}, y, z\right)\rho(x,y,z)\,\mathrm{d}z\,\mathrm{d}x\,\mathrm{d}y\right]\\ &= \frac{2\pi K}{\Delta x\lambda}\left[\iint_{-\infty}^{\infty}\int_s\left[I\left(x - \frac{\Delta x}{2}, y, z\right)\rho(x,y,z) - I\left(x + \frac{\Delta x}{2}, y, z\right)\rho(x,y,z)\right]\mathrm{d}z\,\mathrm{d}x\,\mathrm{d}y\right]\\ &= \frac{2\pi K}{\Delta x\lambda}\left[\iint_{-\infty}^{\infty}\int_s \rho(x,y,z)\left[I\left(x - \frac{\Delta x}{2}, y, z\right) - I\left(x + \frac{\Delta x}{2}, y, z\right)\right]\mathrm{d}z\,\mathrm{d}x\,\mathrm{d}y\right.\end{aligned} \tag{10}$$

In the following sections, the second and third lines of Eq. (10) will be used to calculate $\rho(x, y, z)$ in frequency space, given $I(x, y, z)$ and some knowledge of the flowfield.

III. Relation of Discrete Phase Change to Differential Phase Change via Transfer Function

In this section, the discrete phase change measured by FLDI will be related to a hypothetical, idealized differential FLDI response via transfer functions for the purpose of finding an expression for the density spectrum. Similar to [49,50], to model this hypothetical, idealized FLDI, the separation distance between the beams is reduced to a small value as

$$\frac{\partial\phi}{\partial x} = \lim_{\Delta x \to 0}\frac{\Delta\phi}{\Delta x} \tag{11}$$

Substituting the first line of Eq. (10) into equation Eq. (11) for $\Delta\phi/\Delta x$, we get

$$\frac{\partial\phi}{\partial x} = \lim_{\Delta x\to 0}\left[\frac{2\pi K}{\lambda\Delta x}\left[\iint_{-\infty}^{\infty}\int_s I\left(x-\frac{\Delta x}{2},y,z\right)\rho(x,y,z)\,\mathrm{d}z\,\mathrm{d}x\,\mathrm{d}y - \iint_{-\infty}^{\infty}\int_s I\left(x+\frac{\Delta x}{2},y,z\right)\rho(x,y,z)\,\mathrm{d}z\,\mathrm{d}x\,\mathrm{d}y\right]\right] \tag{12}$$

which reduces to

$$\begin{aligned}\frac{\partial\phi}{\partial x} &= \frac{2\pi K}{\lambda}\left[\iint_{-\infty}^{\infty}\int_s I(x,y,z) \times\left(\lim_{\Delta x\to 0}\frac{\rho[x+(\Delta x/2),y,z]-\rho[x-(\Delta x/2),y,z]}{\Delta x}\right)\mathrm{d}z\,\mathrm{d}x\,\mathrm{d}y\right]\\ &= \frac{2\pi K}{\lambda}\left[\iint_{-\infty}^{\infty}\int_s I(x,y,z)\frac{\partial\rho}{\partial x}\,\mathrm{d}z\,\mathrm{d}x\,\mathrm{d}y\right]\end{aligned} \tag{13}$$

Now, we define the nature of an idealized FLDI instrument by asserting that $\partial\rho/\partial x$ is evaluated at the instrument's focus as

$$\frac{\partial\rho(x,y,z)}{\partial x} \equiv \left.\frac{\partial\rho(x,y,z)}{\partial x}\right|_{x,y,z=0} = \frac{\overline{\partial\rho}}{\partial x} \tag{14}$$

so it is no longer a function of space, and we note that $\int\int_{-\infty}^{\infty} I(x,y,z)\,\mathrm{d}x\mathrm{d}y = 1$. We can then write

$$\frac{\partial\phi}{\partial x} = \frac{2\pi K}{\lambda}\frac{\overline{\partial\rho}}{\partial x}\left[\int_s\iint_{-\infty}^{\infty} I(x,y,z)\,\mathrm{d}x\,\mathrm{d}y\,\mathrm{d}z\right] = \frac{2\pi K}{\lambda}\frac{\overline{\partial\rho}}{\partial x}\int_s \mathrm{d}z \tag{15}$$

The path integration in Eq. (15) introduces a length scale over which the FLDI response is averaged. Here, we approximate the integration length to be equal to the characteristic length of the FLDI probe volume, L_P,

$$\frac{\partial\phi}{\partial x} = \frac{2\pi K L_P}{\lambda}\frac{\overline{\partial\rho}}{\partial x} \tag{16}$$

A spectral analysis of the results is typically of interest, so we solve for $\overline{\partial\rho}/\partial x$ and take the spatial Fourier transform of Eq. (16), as

$$\mathcal{F}\left\{\frac{\overline{\partial\rho}}{\partial x}\right\} = \frac{\lambda}{2\pi K L_P}\mathcal{F}\left\{\frac{\partial\phi}{\partial x}\right\} \tag{17}$$

We compute the Fourier transform of the density using the derivative property of the Fourier transform ($\mathcal{F}\{\partial\rho/\partial x\} = i\kappa\mathcal{F}\{\rho\}$), transforming from physical space to wavenumber (κ) space as

$$\mathcal{F}\{\rho\} = P(\kappa) = \frac{\lambda}{2\pi i\kappa K L_p}\mathcal{F}\left\{\frac{\partial\phi}{\partial x}\right\} \tag{18}$$

In Eq. (19), we define a system transfer function of the FLDI instrument as the ratio of the measured instrument output at the detector to the expected instrument output of an ideal FLDI instrument confined to a specification of our choosing within the framework presented above.

$$H(\kappa) \equiv \frac{[\Delta\phi/\Delta x]_{\text{measured}}}{[\partial\phi/\partial x]_{\text{ideal}}} \tag{19}$$

Using the definition of the transfer function, $H(\kappa)$ we relate the output of the instrument to the first derivative of the phase field. Solving for the derivative of the phase change in Eq. (19), we can make a substitution into Eq. (18) to obtain a relationship in wavenumber space between the measured fluctuations in phase to the actual density fluctuations as

$$\mathcal{F}\{\rho\} = P(\kappa) = \frac{\lambda}{2\pi i\kappa K L_P\Delta x}\frac{\mathcal{F}\{\Delta\phi\}}{H(\kappa)} = \frac{\lambda}{2\pi i\kappa K L_P\Delta x}\frac{\Phi(\kappa)}{H(\kappa)} \tag{20}$$

where $\Phi(\kappa) = \mathcal{F}\{\Delta\phi\}$. In the following sections, a model of the flowfield will be assumed to determine H. It is noted that relating the Fourier transform of density to the phase change in this manner follows [49,50].

IV. Derivation of Transfer Functions

In this section, the transfer functions introduced by [49,50] will be rederived with the framework described in the previous sections. Then, new transfer functions will be introduced that attempt to capture more general flow disturbances, namely, isotropic turbulence. To first rederive the work in [49,50], we assume a sinusoidal disturbance in x, uniform in y, and infinitesimally thin in z at $z = 0$ of the form

$$\rho = \rho(x,y,z) = C\sin(\kappa x+\phi_x)\delta(z) \tag{21}$$

where ϕ_x is an arbitrary phase shift along the x direction, C is an arbitrary constant, and $\delta(z)$ is the Dirac delta. Substituting the chosen form of the disturbance into Eq. (10) allows for the evaluation of the line integral as

$$\begin{aligned}\frac{\Delta\phi}{\Delta x} &= \frac{2\pi KC}{\lambda\Delta x}\left[\iint_{-\infty}^{\infty}\sin(\kappa x+\phi_x)\left(I\left(x-\frac{\Delta x}{2},y\right) - I\left(x+\frac{\Delta x}{2},y\right)\right)\mathrm{d}x\,\mathrm{d}y\right]\\ &= \frac{2\pi KC}{\lambda\Delta x}2\sin\left(\frac{\kappa\Delta x}{2}\right)\exp\left(-\frac{w_0^2\kappa^2}{8}\right)\cos(\phi_x)\end{aligned} \tag{22}$$

The integration in Eq. (22) is similar to the sine transform of a Gaussian, so it is readily computed in Wolfram Mathematica here, as is similarly done elsewhere in the paper. To evaluate the transfer function $H(\kappa)$ for this disturbance, we must first evaluate $\partial\phi/\partial x$. Plugging Eq. (21) into Eq. (15) results in

$$\begin{aligned}\frac{\partial\phi}{\partial x} &= \frac{2\pi K}{\lambda}\frac{\overline{\partial\rho}}{\partial x}\int_s \mathrm{d}z = \frac{2\pi KC}{\lambda}\kappa\cos(\kappa x+\phi_x)\delta(z)|_{x,y,z=0}\\ &= \frac{2\pi KC}{\lambda}\kappa\cos(\phi_x)\end{aligned} \tag{23}$$

noting that we choose $\int_s \mathrm{d}z = 1$ to represent the relevant integration length considered with the Dirac delta. The ratio of Eqs. (22) and (23) is the transfer function

$$H(\kappa) = \frac{2}{\kappa\Delta x}\sin\left(\frac{\kappa\Delta x}{2}\right)\exp\left(-\frac{w_0^2\kappa^2}{8}\right) \tag{24}$$

which we note is Eq. (18) in the work of Schmidt and Shepherd [50]. In that work, they formulate their Eq. (18) by combining two separately derived transfer functions, one that accounts for the finite-differencing effects of FLDI, $H_s = 2\sin(\kappa\Delta x/2)/(\kappa\Delta x)$ [their Eq. (17)], and the effects of beam size at best focus, $H_{w,0} = \exp(-w_0^2\kappa^2/8)$ [their Eq. (15)]. Reproducing the result of Schmidt and Shepherd [50] brings confidence to the methodology of deriving transfer functions outlined in this work.

Next, a disturbance field over a finite domain of the form

$$\rho(x,y,z) = \begin{cases} C\sin(\kappa x+\phi_x) & -L\le z\le L\\ 0 & \text{otherwise}\end{cases} \tag{25}$$

is considered (Fig. 2a). Substituting the chosen form of the disturbance into Eq. (10) yields

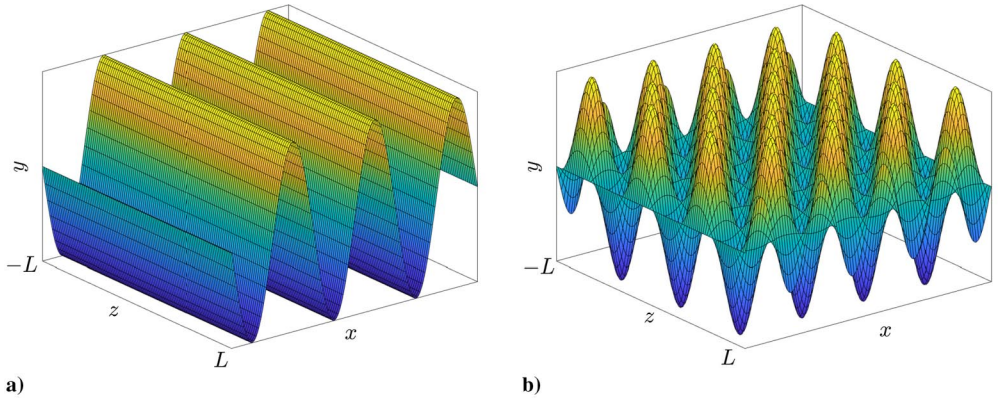

Fig. 2 Representation of density disturbance fields of the form a) $\rho = \rho(x,y,z) = \sin(\kappa x + \phi_x)$ and b) $\rho = \rho(x,y,z) = \sin(\kappa x + \phi_x)\sin(\kappa y + \phi_y)$.

$$\frac{\Delta\phi}{\Delta x} = \frac{2\pi KC}{\Delta x\lambda}\int_{-L}^{L}\iint_{-\infty}^{\infty}\sin(\kappa x + \phi_x)\left[I\left(x - \frac{\Delta x}{2}, y, z\right) - I\left(x + \frac{\Delta x}{2}, y, z\right)\right]\mathrm{d}x\,\mathrm{d}y\,\mathrm{d}z$$
$$= \frac{2\pi KC}{\Delta x\lambda}2\sin\left(\frac{\kappa\Delta x}{2}\right)\cos(\phi_x)\int_{-L}^{L}\exp\left(-\frac{w(z)^2\kappa^2}{8}\right)\mathrm{d}z$$
$$= \frac{2\pi KC}{\Delta x\lambda}2\sin\left(\frac{\kappa\Delta x}{2}\right)\cos(\phi_x)\frac{2\sqrt{2}\pi^{3/2}w_0}{\kappa\lambda} \times \exp\left(-\frac{w_0^2\kappa^2}{8}\right)\mathrm{erf}\left[\frac{L\kappa\lambda}{2\sqrt{2}\pi w_0}\right] \tag{26}$$

Plugging Eq. (25) into Eq. (15) results in

$$\frac{\partial\phi}{\partial x} = \frac{2\pi K}{\lambda}\frac{\overline{\partial\rho}}{\partial x}\int_s \mathrm{d}z = \frac{2\pi KC}{\lambda}\kappa\cos(\kappa x + \phi_x)|_{x,y,z=0}\int_{-L}^{L}\mathrm{d}z$$
$$= \frac{2\pi KC}{\lambda}2L\kappa\cos(\phi_x) \tag{27}$$

noting that L is chosen as the bound on the path integral. The ratio of Eqs. (26) and (27) is the transfer function

$$H(\kappa) = \frac{2\sqrt{2}\pi^{3/2}w_0}{\kappa^2\lambda\Delta x L}\sin\left(\frac{\kappa\Delta x}{2}\right)\exp\left(-\frac{w_0^2\kappa^2}{8}\right)\mathrm{erf}\left[\frac{L\kappa\lambda}{2\sqrt{2}\pi w_0}\right] \tag{28}$$

which is similar to a combination of Eqs. (16) and (17) in the work of Schmidt and Shepherd [50]. Equation (28) may be used as a transfer function for disturbances within a wind tunnel with walls from $-L$ to L. However, assuming that a disturbance has the structure of Eq. (25) may not be the best representation of a real flowfield as L becomes large relative to $1/\kappa$.

Also note that when taking the ratio of Eqs. (26) and (27), it is arbitrary to choose the integration limits of the idealized FLDI system as $\pm L$ in Eq. (27), which results in an L in the denominator of Eq. (28). That is, for a given disturbance field, we can relate the phase response of the actual FLDI system [represented by Eq. (26)] to the phase response of an idealized FLDI system having an integration length of one's choosing. One convenient choice would be $-L_P$ to L_P, noting that L_P is the characteristic length of the FLDI probe volume in Eq. (20). Equation (28) then becomes

$$H(\kappa) = \frac{2\sqrt{2}\pi^{3/2}w_0}{\kappa^2\lambda\Delta x L_P}\sin\left(\frac{\kappa\Delta x}{2}\right)\exp\left(-\frac{w_0^2\kappa^2}{8}\right)\mathrm{erf}\left[\frac{L\kappa\lambda}{2\sqrt{2}\pi w_0}\right] \tag{29}$$

Importantly, setting the integration length to be the characteristic length of the FLDI instrument in Eq. (27) eliminates the need to characterize L_P, as it cancels out in Eq. (20) when it is applied to reduce FLDI data.

Disturbances of increasingly complex form will now be introduced. First, to model isotropic turbulence with disturbances in x and y at the focus of the FLDI system, the density is assumed to take the form

$$\rho = \rho(x,y,z) = C\sin(\kappa x + \phi_x)\sin(\kappa y + \phi_y)\delta(z) \tag{30}$$

Substituting the chosen form of the disturbance into Eq. (10) yields

$$\frac{\Delta\phi}{\Delta x} = \frac{2\pi KC}{\Delta x\lambda}\iint_{-\infty}^{\infty}\sin(\kappa x + \phi_x)\sin(\kappa y + \phi_y)\left[I\left(x - \frac{\Delta x}{2}, y, z\right) - I\left(x + \frac{\Delta x}{2}, y, z\right)\right]\mathrm{d}x\,\mathrm{d}y$$
$$= \frac{2\pi KC}{\Delta x\lambda}2\sin\left(\frac{\kappa\Delta x}{2}\right)\exp\left(-\frac{w_0^2\kappa^2}{4}\right)\cos(\phi_x)\sin(\phi_y) \tag{31}$$

Plugging Eq. (30) into Eq. (15) results in

$$\frac{\partial\phi}{\partial x} = \frac{2\pi K}{\lambda}\frac{\overline{\partial\rho}}{\partial x}\int_s \mathrm{d}z$$
$$= \frac{2\pi KC}{\lambda}\kappa\cos(\kappa x + \phi_x)\sin(\kappa y + \phi_y)\delta(z)|_{x,y,z=0}$$
$$= \frac{2\pi KC}{\lambda}\kappa\cos(\phi_x)\sin(\phi_y) \tag{32}$$

The ratio of Eqs. (31) and (32) is the transfer function

$$H(\kappa) = \frac{2}{\kappa\Delta x}\sin\left(\frac{\kappa\Delta x}{2}\right)\exp\left(-\frac{w_0^2\kappa^2}{4}\right) \tag{33}$$

noting that the only change between Eqs. (33) and (24) is the factor of two in the exponential.

Next, consider an isotropic disturbance field (see Fig. 2b) of the form

$$\rho(x,y,z) = \begin{cases} C\sin(\kappa x + \phi_x)\sin(\kappa y + \phi_y) & -L \le z \le L \\ 0 & \text{otherwise} \end{cases} \tag{34}$$

which, following the above process, yields

$$\frac{\Delta\phi}{\Delta x} = \frac{2\pi KC}{\Delta x\lambda}\int_{-L}^{L}\iint_{-\infty}^{\infty}\sin(\kappa x+\phi_x)\sin(\kappa y+\phi_y)\left[I\left(x-\frac{\Delta x}{2},y,z\right)\right.$$
$$\left. - I\left(x+\frac{\Delta x}{2},y,z\right)\right]\mathrm{d}x\,\mathrm{d}y\,\mathrm{d}z$$
$$= \frac{2\pi KC}{\Delta x\lambda}2\sin\left(\frac{\kappa\Delta x}{2}\right)\cos(\phi_x)\sin(\phi_y)\int_{-L}^{L}\exp\left(-\frac{w(z)^2\kappa^2}{4}\right)\mathrm{d}z$$
$$= \frac{2\pi KC}{\Delta x\lambda}2\sin\left(\frac{\kappa\Delta x}{2}\right)\cos(\phi_x)\sin(\phi_y)\frac{2\pi^{3/2}w_0}{\kappa\lambda}\exp$$
$$\left(-\frac{w_0^2\kappa^2}{4}\right)\mathrm{erf}\left[\frac{L\kappa\lambda}{2\pi w_0}\right] \tag{35}$$

Plugging Eq. (34) into Eq. (15) results in

$$\frac{\partial\phi}{\partial x} = \frac{2\pi K}{\lambda}\frac{\overline{\partial\rho}}{\partial x}\int_s \mathrm{d}z = \frac{2\pi KC}{\lambda}\kappa\cos(\kappa x+\phi_x)\sin(\kappa y+\phi_y)|_{x,y,z=0}\int_{-L}^{L}\mathrm{d}z$$
$$= \frac{2\pi KC}{\lambda}2L\kappa\cos(\phi_x)\sin(\phi_y) \tag{36}$$

and taking the ratio of Eqs. (35) and (36) gives the transfer function

$$H(\kappa) = \frac{2\pi^{3/2}w_0}{\kappa^2\lambda\Delta xL}\sin\left(\frac{\kappa\Delta x}{2}\right)\exp\left(-\frac{w_0^2\kappa^2}{4}\right)\mathrm{erf}\left[\frac{L\kappa\lambda}{2\pi w_0}\right] \tag{37}$$

Finally, in terms of considering disturbances within a fixed boundary L, we consider a three-dimensional isotropic disturbance field of the form

$$\rho(x,y,z) = \begin{cases} C\sin(\kappa x+\phi_x)\sin(\kappa y+\phi_y)\sin(\kappa z+\phi_z) & -L\le z\le L \\ 0 & \text{otherwise} \end{cases} \tag{38}$$

Plugging this disturbance into the phase change relation yields

$$\frac{\Delta\phi}{\Delta x} = \frac{2\pi KC}{\Delta x\lambda}\int_{-L}^{L}\iint_{-\infty}^{\infty}\sin(\kappa x+\phi_x)\sin(\kappa y+\phi_y)\sin(\kappa z$$
$$+\phi_z)\left[I\left(x-\frac{\Delta x}{2},y,z\right)-I\left(x+\frac{\Delta x}{2},y,z\right)\right]\mathrm{d}x\mathrm{d}y\mathrm{d}z$$
$$= \frac{2\pi KC}{\Delta x\lambda}2\sin\left(\frac{\kappa\Delta x}{2}\right)\cos(\phi_x)\sin(\phi_y)\int_{-L}^{L}\sin(\kappa z$$
$$+\phi_z)\exp\left(-\frac{w(z)^2\kappa^2}{4}\right)\mathrm{d}z$$
$$= \frac{2\pi KC}{\Delta x\lambda}2\sin\left(\frac{\kappa\Delta x}{2}\right)\cos(\phi_x)\sin(\phi_y)\sin(\phi_z)\frac{i\pi^{3/2}w_0}{\kappa\lambda}\exp$$
$$\left[-\frac{w_0^2}{4}\left(\kappa^2+\frac{4\pi^2}{\lambda^2}\right)\right]\times\left[\mathrm{erfi}\left[\frac{\pi w_0}{\lambda}-\frac{iL\kappa\lambda}{2\pi w_0}\right]-\mathrm{erfi}\left[\frac{\pi w_0}{\lambda}+\frac{iL\kappa\lambda}{2\pi w_0}\right]\right] \tag{39}$$

noting that erf and erfi are the error function and imaginary error function, respectively. Following the same procedure that was used to obtain Eq. (37), the transfer function for this disturbance field is

$$H(\kappa) = \frac{i\pi^{3/2}w_0}{\kappa^2\lambda\Delta xL}\exp\left[-\frac{w_0^2}{4}\left(\kappa^2+\frac{4\pi^2}{\lambda^2}\right)\right]\sin\left(\frac{\kappa\Delta x}{2}\right)\left[\mathrm{erfi}\left[\frac{\pi w_0}{\lambda}\right.\right.$$
$$\left.\left. - \frac{iL\kappa\lambda}{2\pi w_0}\right] - \mathrm{erfi}\left[\frac{\pi w_0}{\lambda}+\frac{iL\kappa\lambda}{2\pi w_0}\right]\right] \tag{40}$$

This expression is simplified using the identities $i\times\mathrm{erfi}(z) = \mathrm{erf}(i\times z)$, $\mathrm{erf}(-z) = -\mathrm{erf}(z)$, and $2\Re[\mathrm{erf}(x+i\times y)] = \mathrm{erf}(x+i\times y)+\mathrm{erf}(x-i\times y)$ with $x = L\kappa\lambda/2\pi w_0$ and $y = \pi w_0/\lambda$. With this, Eq. (40) becomes

$$H(\kappa) = \frac{\pi^{3/2}w_0}{\kappa^2\lambda\Delta xL}\exp\left[-\frac{w_0^2}{4}\left(\kappa^2\right.\right.$$
$$\left.\left.+\frac{4\pi^2}{\lambda^2}\right)\right]\sin\left(\frac{\kappa\Delta x}{2}\right)\left[2\Re\left[\mathrm{erf}\left[\frac{i\pi w_0}{\lambda}+\frac{L\kappa\lambda}{2\pi w_0}\right]\right]\right] \tag{41}$$

Note that the L in the denominator in Eq. (37) or Eq. (41) could be written as L_P, as shown in Eq. (29).

As an alternative to considering disturbances within a fixed boundary, L, we can assume a sinusoidal disturbance in x, with a Gaussian width σ as

$$\rho = \rho(x,y,z) = C\sin(\kappa x+\phi_x)\exp\left(-\frac{y^2+z^2}{\sigma^2}\right) \tag{42}$$

This model may be useful to determine the response of an FLDI system to a axisymmetric turbulent jet of width σ issuing in the x direction centered at $y = z = 0$. Plugging this form of the disturbance into the phase-change relation, we get

$$\frac{\Delta\phi}{\Delta x} = \frac{2\pi KC}{\Delta x\lambda}\int_{-\infty}^{\infty}\iint_{-\infty}^{\infty}\sin(\kappa x+\phi_x)\exp\left(-\frac{y^2+z^2}{\sigma^2}\right)\left[I\left(x-\frac{\Delta x}{2},y,z\right)\right.$$
$$\left. - I\left(x+\frac{\Delta x}{2},y,z\right)\right]\mathrm{d}x\mathrm{d}y\mathrm{d}z$$
$$= \frac{2\pi KC}{\Delta x\lambda}2\sin\left(\frac{\kappa\Delta x}{2}\right)\cos(\phi_x)\int_{-\infty}^{\infty}\frac{1}{\sqrt{[w(z)^2/2\sigma^2]+1}}\exp$$
$$\left(-\frac{w(z)^2\kappa^2}{8}\right)\exp\left(\frac{-z^2}{\sigma^2}\right)\mathrm{d}z,$$
$$= \frac{2\pi KC}{\Delta x\lambda}2\sin\left(\frac{\kappa\Delta x}{2}\right)\cos(\phi_x)\int_{-\infty}^{\infty}\exp\left(-\frac{w(z)^2\kappa^2}{8}\right)\exp\left(\frac{-z^2}{\sigma^2}\right)\mathrm{d}z,$$
$$= \frac{2\pi KC}{\Delta x\lambda}2\sin\left(\frac{\kappa\Delta x}{2}\right)\cos(\phi_x)\frac{4\pi^{3/2}\exp[-(1/8)\kappa^2w_0^2]}{\sqrt{(\kappa^2\lambda^2/2w_0^2)+(4\pi^2/\sigma^2)}} \tag{43}$$

To make the integration in z on the second line of Eq. (43) tractable, we assume that the jet width is much larger than the beam waist, $\sigma \gg w(z)$. Plugging Eq. (42) into Eq. (15) results in

$$\frac{\partial\phi}{\partial x} = \frac{2\pi K}{\lambda}\frac{\overline{\partial\rho}}{\partial x}\int_s \mathrm{d}z$$
$$= \frac{2\pi KC}{\lambda}\kappa\cos(\kappa x+\phi_x)\exp\left(-\frac{y^2+z^2}{\sigma^2}\right)\Big|_{x,y,z=0}\int_{-\sigma}^{\sigma}\mathrm{d}z \tag{44}$$
$$= \frac{2\pi KC}{\lambda}2\sigma\kappa\cos(\phi_x)$$

and taking the ratio of Eqs. (42–44), the transfer function is

$$H(\kappa) = \frac{2\pi^{3/2}\sin(\kappa\Delta x/2)\exp[-(1/8)\kappa^2w_0^2]}{\sigma\kappa\Delta x\sqrt{(\kappa^2\lambda^2/2w_0^2)+(4\pi^2/\sigma^2)}} \tag{45}$$

For an increasingly complex disturbance in x and y with a Gaussian width σ as

$$\rho = \rho(x,y,z) = C\sin(\kappa x+\phi_x)\sin(\kappa y+\phi_y)\exp\left(-\frac{y^2+z^2}{\sigma^2}\right) \tag{46}$$

yields

$$H(\kappa) = \frac{2\pi^{3/2}\sin(\kappa\Delta x/2)\exp[-(1/4)\kappa^2w_0^2]}{\sigma\kappa\Delta x\sqrt{(\kappa^2\lambda^2/2w_0^2)+(4\pi^2/\sigma^2)}} \tag{47}$$

following the above procedure and assumptions. Finally, assuming a disturbance of the form

$$\rho = \rho(x,y,z)$$
$$= C\sin(\kappa x+\phi_x)\sin(\kappa y+\phi_y)\sin(\kappa z+\phi_z)\exp\left(-\frac{y^2+z^2}{\sigma^2}\right) \quad (48)$$

yields

$$H(\kappa) = \frac{2\pi^{3/2}\sin(\kappa\Delta x/2)\exp\left\{-(1/4)w_0^2\kappa^2\left[1+(4\pi^2\sigma^2/(4\pi^2w_0^2+\kappa^2\lambda^2\sigma^2))\right]\right\}}{\kappa\Delta x\sigma\sqrt{\kappa^2\lambda^2/w_0^2+4\pi^2/\sigma^2}} \quad (49)$$

For each of the transfer functions pertaining to the axisymmetric jet, Eqs. (45), (47), and (49), the FLDI user must acknowledge that one is integrating and averaging through the spanwise structure of the jet in the z direction.

V. Experimental Setup

An FLDI setup was constructed to probe a turbulent jet. To construct the FLDI system, the linearly polarized laser beam produced by a Cobolt 05-01 series laser is expanded using a diverging lens. The expanding beam is then passed through the two available diffractive optics to generate a grid of beams six columns wide in the streamwise x direction and two rows tall in the y direction. The collection of beams is then circularly polarized by a quarter-wave plate before being split once more in the streamwise direction by a Wollaston prism. Wollaston prisms of three different separation angles were used for these experiments: 0.5 arcminute, 1 arcminute, and 2 arcminutes. The 12 orthogonally polarized beam pairs probe the jet exit flow. The beam pairs generated by the upbeam Wollaston prism are recombined by a Wollaston prism of equivalent separation angle on the downbeam side. The interference caused by the individual beams within each beam pair traversing different OPLs is manifested as fluctuations in the intensity of the recombined beams and measured as changes in voltage by photodetectors. For these experiments, measurements from 2 of the 12 beam pairs are presented. A schematic of the setup is presented in Fig. 3.

A picture of the beam inter- and intraspacing generated using a 2-arcminute Wollaston prism is presented in Fig. 4. The beam interspacing was 1.639 mm, and the beam intraspacing was 262.53 μm. The beam interspacing did not change appreciably for the other Wollaston prisms used in this experimental campaign. The beam intraspacing using the 1-arcminute Wollaston prism was 85.20 μm, and the intraspacing using the 0.5-arcminute Wollaston prism was 36.34 μm.

A round, sonic free-jet was used to generate the turbulent disturbance field being probed by the FLDI beams. The free-jet was generated in a laboratory setting. Compressed air was regulated to approximately 30 PSIG in the reservoir of a nozzle with an exit diameter of 3.7 mm. The nozzle was mounted on a platform that allowed for independent and precise adjustment in the x, y, and z directions. For these experiments, the nozzle was positioned at the focus ($z = 0$), 43 mm ($x/D = 11.6$) away from the FLDI beam pairs.

VI. Results

Results from the experiments are presented in this section. First, a temporal correlation between the two closely spaced FLDI probes yields the dispersion relation, $\kappa = 2\pi f/c_p(f)$. The phase speed $c_p(f)$ was determined following a procedure similar to the one described by Ceruzzi et al. [56]. For these experiments, an inverse tangent function provided the most natural fit to the discretely calculated convective velocities and resulted in a functional relationship of the data points. Figure 5 shows the dispersion relation fits for convective velocities measured with a 0.5-, 1-, and 2-arcminute Wollaston prism. It demonstrates the dependency between the disturbance convective velocity and the frequency. That is, the disturbances propagating at higher convective velocities tend to fluctuate at higher frequencies. For this flowfield, the similarity between the dispersion relations generated using the three Wollaston prisms also demonstrates the independency of the measured dispersion to the optical setup.

Figure 6 shows the transfer functions for the experiment using a 0.5-arcminute Wollaston prism. For the current experiments, the length scale in the transfer function ($2L$ or σ) is relatively small, and so the transfer function modifies the spectrum most at relatively high wavenumber. The transfer functions of three-dimensional

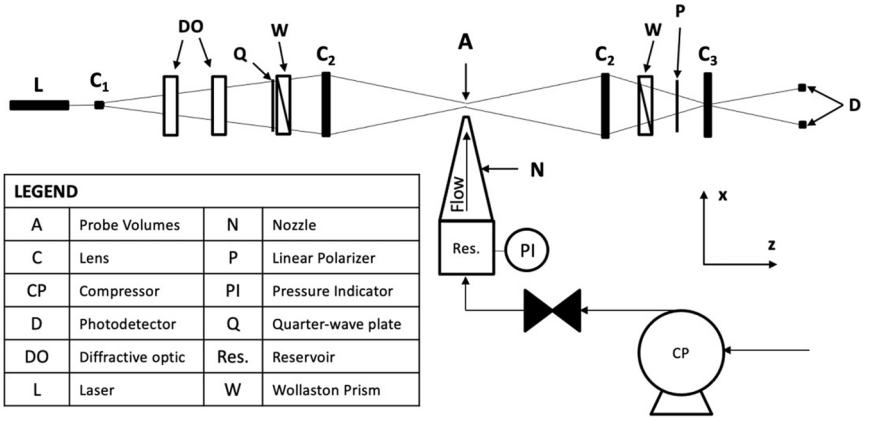

LEGEND			
A	Probe Volumes	N	Nozzle
C	Lens	P	Linear Polarizer
CP	Compressor	PI	Pressure Indicator
D	Photodetector	Q	Quarter-wave plate
DO	Diffractive optic	Res.	Reservoir
L	Laser	W	Wollaston Prism

Fig. 3 Schematic of FLDI setup used to probe the exit of a turbulent jet.

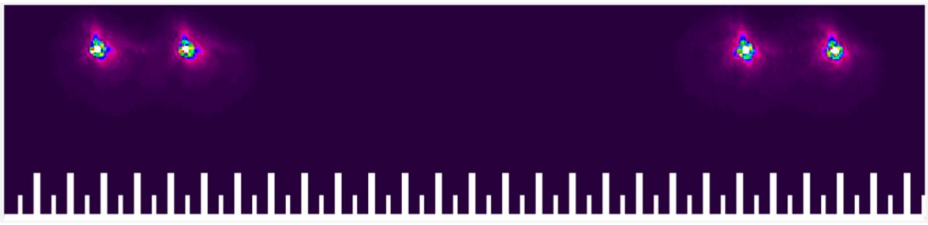

Fig. 4 FLDI beam pairs for a setup developed using diffractive optics and a 2-arcminute Wollaston prism. The major tick marks are at 100 μm, and the minor tick marks are at 50 μm.

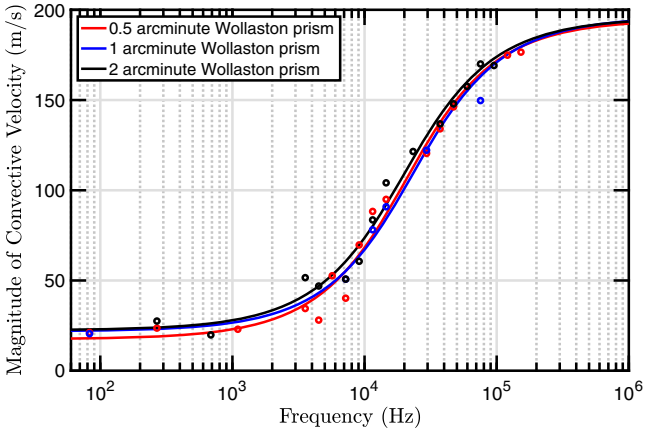

Fig. 5 Convective velocities and fits of dispersion relation for experiments with 0.5-, 1-, and 2-arcminute Wollaston prisms.

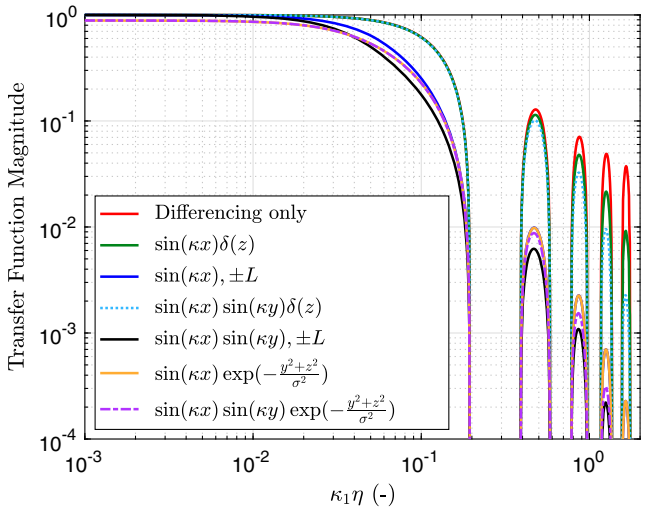

Fig. 6 Calculated transfer functions for an experiment with 0.5-arcminute Wollaston prism. Here, κ_1 refers to the wavenumber of the streamwise fluctuations.

disturbance fields [Eqs. (41) and (49)] suffer from a steep drop in magnitude at a much earlier than expected value of $\kappa_1\eta$, and are not presented in this figure. Their poor behavior most likely stems from the assumption that the disturbances are perfectly correlated along the z direction. We will continue to investigate these transfer functions and will present our findings in future work. Although the disturbances in x and y are also not perfectly correlated, as the simpler one-dimensional and two-dimensional transfer functions assume, the ratio of the disturbance length scale to the integration length is less problematic. That is, $1/\kappa$ is closer in length scale to the beam waist $w(z)$ (for x and y integration) than it is to L (for z integration). This is an apparent limitation of the present approach where we have assumed that disturbances are isotropic and perfectly correlated in all directions.

Here, the one-dimensional energy spectra of the density fluctuations are defined to be the one-dimensional Fourier transform of the autocorrelation function, $R_{11\rho}(x)$, analogous to the energy spectrum formed from velocity fluctuations in the work of Pope [57]. Unfortunately, the autocorrelation function in x space is not directly available from FLDI data because of the presence of dispersion (Fig. 5); that is, Taylor's hypothesis may not be applicable in the present jet experiments. Additionally, the FLDI spectra need to be analyzed in wavenumber space so that the transfer functions may be applied. The Wiener–Khinchin theorem provides a direct relationship between the Fourier transform of the density fluctuations to the autocorrelation function, and it is used to write the energy spectra of the density fluctuations as

$$E_{11\rho}(\kappa_1) = \mathcal{F}\{R_{11\rho}(x)\} = \mathcal{F}\{\rho(x)\}\mathcal{F}\{\rho(x)\}^* = P(\kappa)P(\kappa)^* \quad (50)$$

where the asterisk $(*)$ denotes the complex conjugate and $P(\kappa)$ is the discrete Fourier spectrum of density fluctuations per Eq. (20) as calculated with the "fft" function in MATLAB. Note that the transfer function alters the energy spectra as $E_{11}(\kappa) \sim H(\kappa)^{-2}$. One can calculate $E_{11\rho}$ from built-in power-spectral density (PSD) estimation functions in MATLAB, for example, but the researcher must take care when considering the units; factors of $2, \pi$, and the period of the signal may appear unintentionally when using built-in PSD functions, which will make the amplitude different from Eq. (50). A standard check is to compute $\overline{\rho^2} = \int E_{11\rho}(\kappa_1)\,\mathrm{d}\kappa$ for different processing methods to build confidence in the results.

Results for the experiment with a 0.5-arcminute Wollaston prism are presented in Fig. 7. The figure shows the response of one of the FLDI beams in the dual-FLDI beam pair, corrected by the transfer functions corresponding to the disturbance fields as labeled. The spectra are offset by a multiple of two from one another along the ordinate for clarity. The model spectrum labeled $E_{11}(\kappa_1)$ in Fig. 7 is the one-dimensional turbulence spectrum given by

$$E_{11}(\kappa_1) = \int_{\kappa_1}^{\infty} \frac{E(\kappa)}{\kappa}\left(1 - \frac{\kappa_1^2}{\kappa^2}\right) d\kappa$$

from Pope [57]. The results indicate that, as the complexity of the modeled disturbance better matches the actual disturbance field, the corrected one-dimensional energy spectra of the density fluctuations more closely match the model spectrum. The transfer functions represent a means to account for the differencing nature of FLDI [$1/\kappa$ in Eq. (20)] as well as the response of the FLDI where the disturbance wavenumber, beam size, and overlapping beam area all are on the same order near the focus by introducing spectral components (e.g., $\sin(\kappa x)$). In all cases, the inertial subrange is of the $-5/3$ slope hypothesized by Kolmogorov. For idealized disturbance fields, where the disturbance in space approaches the limit of infinitely small fluctuations, of the form $\sin(\kappa x)\delta(z)$ or $\sin(\kappa x)\sin(\kappa y)\delta(z)$, the corrections yield an inertial subrange that is shortened by approximately half a decade, resulting in the transition to the dissipation range occurring earlier than expected when compared to the modeled one-dimensional energy spectrum. When the disturbance field more realistically occupies a physical length (2L or σ), the corrections by the appropriate transfer functions broaden the inertial subrange. Due to poor experimental design, the beginning of the dissipation range is

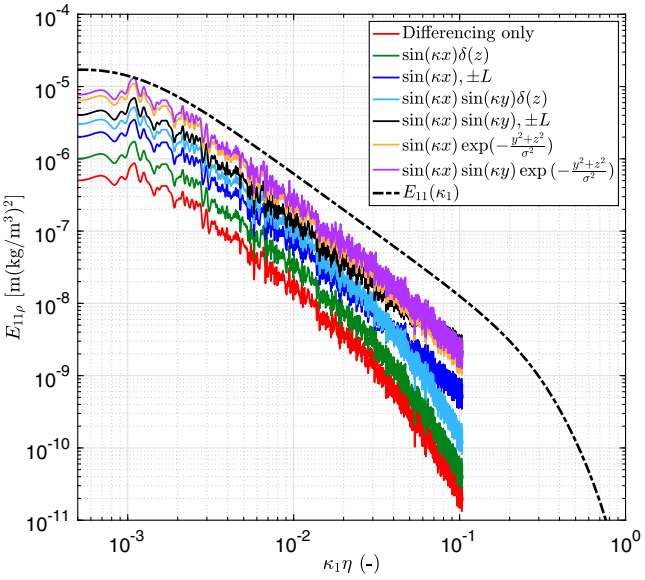

Fig. 7 One-dimensional energy spectra of the density fluctuations for an experiment performed with a round turbulent jet, corrected by transfer functions for disturbance fields as labeled.

not visible for these spectra; a smaller FLDI beam intraspacing would be necessary to process the spectra beyond $\kappa_1\eta \approx 0.1$.

VII. Conclusions

In this work, a model of FLDI is derived by incorporating the local intensity of each beam in an FLDI beam pair. The resulting transfer functions represent a means to account for the differencing nature of FLDI [$1/\kappa$ in Eq. (20)] as well as the response of the FLDI where the disturbance wavenumber, beam size, and overlapping beam area all are on the same order near the focus by introducing spectral components (e.g., $\sin(\kappa x)$). This strategy enabled the rederivation of some transfer functions to reduce FLDI data originally found in [49,50]. Additional transfer functions were derived for increasingly complex disturbance fields that account for disturbances fluctuating not only in the streamwise direction, x, but also the additional y and z directions, orthogonal to the flow. For the transfer functions derived for a finite boundary, $-L$ to L, it was identified that the length scale for the $\partial\phi/\partial x$ evaluation was a choice. That is, a strategic choice of the integration limits for evaluating $\partial\phi/\partial x$ in the denominator of the transfer function enabled the cancelation of L_P when the transfer function was applied, thus simplifying FLDI data reduction.

By performing experiments with a round, turbulent jet and reducing the data using the derived transfer functions, it was shown that increasing the complexity of the transfer function has merit. When the disturbance modeled by the transfer function better matches the actual disturbance field, the results obtained from the FLDI system more closely align with a well-established model and published data. The best results were obtained when modeling the field to include disturbances in x and y over a physical length scale in z, be it $2L$ or σ. However, modeling the field to include disturbances in z resulted in a transfer function that did not yield meaningful results, most likely due to assumptions about the correlation of disturbances along that integration direction. An alternate treatment where the disturbances are considered in a statistical manner, perhaps a Gaussian random field, could address this issue.

Acknowledgments

Support for this work was provided by the Air Force Office of Scientific Research (AFOSR) Grants FA9550-16-1-0262 and FA9550-18-1-0403; Sarah Popkin of AFOSR is the Program Manager for both grants.

References

[1] Smeets, G., and George, A., "Gas Dynamic Investigations in a Shock Tube Using a Highly Sensitive Interferometer," Translation of ISL Internal Rept. 14/71, Institut franco-allemand de recherches de Saint-Louis, Saint-Louis, France, Original 1971, Translation 1996.

[2] Smeets, G., "Laser Interferometer for High Sensitivity Measurements on Transient Phase Objects," *IEEE Transactions on Aerospace and Electronic Systems*, Vol. AES-8, No. 2, 1972, pp. 186–190. https://doi.org/10.1109/TAES.1972.309488

[3] Smeets, G., and George, A., "Anwendungen des Laser-Differentialinterferometers in der Gasdynamik," ISL—N 28/73, Institut franco-allemand de recherches de Saint-Louis, Saint-Louis, France, Also translated by A. Goetz, ADA-307459, 1973.

[4] Smeets, G., "Laser-Interferometer mit grossen, fokussierten Lichtbündeln für lokale Messungen," ISL—N 11/73, Institut franco-allemand de recherches de Saint-Louis, Saint-Louis, France, 1973.

[5] Smeets, G., "Verwendung eines Laser-Differentialinterferometers zur Bestimmung lokaler Schwankungsgrössen sowie des mittleren Dichteprofils in cinem turbulenten Freistrahl," ISL—N 20/74, Institut franco-allemand de recherches de Saint-Louis, Saint-Louis, France, 1974.

[6] Smeets, G., "Flow Diagnostics by Laser Interferometry," *IEEE Transactions on Aerospace and Electronic Systems*, Vol. AES-13, No. 2, 1977, pp. 82–90. https://doi.org/10.1109/TAES.1977.308441

[7] Smeets, G., and George, A., "Laser Differential Interferometer Applications in Gas Dynamics," Translation of ISL Internal Rept. 28/73, Institut franco-allemand de recherches de Saint-Louis, Saint-Louis, France, Original 1975, Translation 1996.

[8] Laderman, A. J., and Demetriades, A., "Detection of Boundary Layer-Transition with a Laser Beam," *AIAA Journal*, Vol. 14, No. 1, 1976, pp. 102–104. https://doi.org/10.2514/3.7058

[9] Azzazy, M., Modarress, D., and Hoeft, T., "High Sensitivity Boundary Layer Transition Detector," *Proceedings of SPIE Vol. 569 High Speed Photography, Videography, and Photonics I/I*, SPIE, San Diego, CA, 1985, pp. 64–73. https://doi.org/10.1117/12.949865

[10] Azzazy, M., Modarress, D., and Trolinger, J. D., "Feasibility Study of Optical Boundary Layer Transition Detection Method," NASA CR-178109, 1986.

[11] Azzazy, M., Modarress, D., and Hoeft, T., "High-Sensitivity Density Fluctuation Detector," *Journal of Physics E: Scientific Instruments*, Vol. 20, No. 4, 1987, p. 428. https://doi.org/10.1088/0022-3735/20/4/017

[12] O'Hare, J. E., "A Nonperturbing Boundary-Layer Transition Detector," *Proceedings of SPIE 0569, High Speed Photography, Videography, and Photonics III*, SPIE, San Diego, CA, 1985, pp. 58–63. https://doi.org/10.1117/12.949864

[13] Collicott, S. H., Schneider, S. P., and Messersmith, N. L., "Review of Optical Diagnostic Methods for Hypersonic Low-Noise Facilities," *Proceedings of 34th Aerospace Sciences Meeting and Exhibit*, AIAA Paper 1996-0851, 1996. https://doi.org/10.2514/6.1996-851

[14] Salyer, T. R., Randall, L. R., Collicott, S. H., and Schneider, S. P., "Use of Laser Differential Interferometry to Study Receptivity on a Hemispherical Nose at Mach 4," *Proceedings of 36th AIAA Aerospace Sciences Meeting and Exhibit*, AIAA Paper 1998-0238, 1998. https://doi.org/10.2514/6.1998-238

[15] Salyer, T. R., Collicott, S. H., and Schneider, S. P., "Feedback Stabilized Laser Differential Interferometry for Supersonic Blunt Body Receptivity Experiments," *Proceedings of 38th Aerospace Sciences Meeting and Exhibit*, AIAA Paper 2000-0416, 2000. https://doi.org/10.2514/6.2000-416

[16] Salyer, T. R., "Laser Differential Interferometry for Supersonic Blunt Body Receptivity Experiments," Ph.D. Thesis, Purdue Univ., West Lafayette, IN, 2002.

[17] Salyer, T. R., Collicott, S. H., and Schneider, S. P., "Characterizing Laser-Generated Hot Spots for Receptivity Studies," *AIAA Journal*, Vol. 44, No. 12, 2006, p. 2871–2878. https://doi.org/10.2514/1.13023

[18] Parziale, N. J., Shepherd, J. E., and Hornung, H. G., "Reflected Shock Tunnel Noise Measurement by Focused Differential Interferometry," *Proceedings of 42nd AIAA Fluid Dynamics Conference and Exhibit*, AIAA Paper 2012-3261, 2012. https://doi.org/10.2514/6.2012-3261

[19] Parziale, N. J., Jewell, J. S., Shepherd, J. E., and Hornung, H. G., "Optical Detection of Transitional Phenomena on Slender Bodies in Hypervelocity Flow," *Proceedings of RTO Specialists Meeting AVT-200/RSM-030 on Hypersonic Laminar-Turbulent Transition*, NATO, San Diego, CA, 2012.

[20] Parziale, N. J., Shepherd, J. E., and Hornung, H. G., "Differential Interferometric Measurement of Instability at Two Points in a Hypervelocity Boundary Layer," *Proceedings of 51st AIAA Aerospace Sciences Meeting Including the New Horizons Forum and Aerospace Exposition*, AIAA Paper 2013-0521, 2013. https://doi.org/10.2514/6.2013-521

[21] Parziale, N. J., Shepherd, J. E., and Hornung, H. G., "Differential Interferometric Measurement of Instability in a Hypervelocity Boundary Layer," *AIAA Journal*, Vol. 51, No. 3, 2013, pp. 750–753. https://doi.org/10.2514/1.J052013

[22] Parziale, N. J., "Slender-Body Hypervelocity Boundary-Layer Instability," Ph.D. Thesis, California Inst. of Technology, Pasadena, CA, 2013.

[23] Parziale, N. J., Shepherd, J. E., and Hornung, H. G., "Free-Stream Density Perturbations in a Reflected-Shock Tunnel," *Experiments in Fluids*, Vol. 55, No. 2, 2014, p. 1665. https://doi.org/10.1007/s00348-014-1665-0

[24] Parziale, N. J., Shepherd, J. E., and Hornung, H. G., "Observations of Hypervelocity Boundary-Layer Instability," *Journal of Fluid Mechanics*, Vol. 781, Sept. 2015, pp. 87–112. https://doi.org/10.1017/jfm.2015.489

[25] Jewell, J. S., Parziale, N. J., Lam, K.-L., Hagen, B. J., and Kimmel, R. L., "Disturbance and Phase Speed Measurements for Shock Tubes and Hypersonic Boundary-Layer Instability," *Proceedings of 32nd AIAA Aerodynamic Measurement Technology and Ground Testing Conference*, AIAA Paper 2016-3112, 2016. https://doi.org/10.2514/6.2016-3112

[26] Jewell, J. S., Hameed, A., Parziale, N. J., and Gogineni, S. P., "Disturbance Speed Measurements in a Circular Jet via Double Focused Laser Differential Interferometry," *Proceedings of AIAA Scitech 2019*, AIAA

Paper 2019-2293, 2019.
https://doi.org/10.2514/6.2019-2293
[27] Ceruzzi, A. P., and Cadou, C. P., "Simultaneous Velocity and Density Gradient Measurements Using Two-Point Focused Laser Differential Interferometry," *Proceedings of AIAA Scitech 2019*, AIAA Paper 2019-2295, 2019.
https://doi.org/10.2514/6.2019-2295
[28] Ceruzzi, A. P., Callis, B., Weber, D., and Cadou, C. P., "Application of Focused Laser Differential Interferometry (FLDI) in a Supersonic Boundary Layer," *Proceedings of AIAA Scitech 2020*, AIAA Paper 2020-1973, 2020.
https://doi.org/10.2514/6.2020-1973
[29] Ceruzzi, A. P., McManamen, B., and Cadou, C. P., "Demonstration of Two-Point Focused Laser Differential Interferometry (2 pFLDI) in a Mach 18 flow," *Proceedings of AIAA Scitech 2021*, AIAA Paper 2021-0983, 2021.
https://doi.org/10.2514/6.2021-0983
[30] Weisberger, J. M., Bathel, B. F., Herring, G. C., King, R. A., Chou, A., and Jones, S. B., "Two-Point Focused Laser Differential Interferometry Second-Mode Measurements at Mach 6," *Proceedings of AIAA Aviation Forum*, AIAA Paper 2019-2903, 2019.
https://doi.org/10.2514/6.2019-2903
[31] Weisberger, J. M., Bathel, B. F., Herring, G. C., Buck, G. M., Jones, S. B., and Cavone, A. A., "Multi-Point Line Focused Laser Differential Interferometer for High-Speed Flow Fluctuation Measurements," *Applied Optics*, Vol. 59, No. 35, 2020, pp. 11,180–11,195.
https://doi.org/10.1364/AO.411006
[32] Bathel, B. F., Weisberger, J. M., Herring, G. C., King, R. A., Jones, S. B., Kennedy, R. E., and Laurence, S. J., "Two-Point, Parallel-Beam Focused Laser Differential Interferometry with a Nomarski Prism," *Applied Optics*, Vol. 59, No. 2, 2020, pp. 244–252.
https://doi.org/10.1364/AO.59.000244
[33] Price, T. J., Gragston, M., Schmisseur, J. D., and Kreth, P. A., "Measurement of Supersonic Jet Screech with Focused Laser Differential Interferometry," *Applied Optics*, Vol. 59, No. 28, 2020, pp. 8902–8908.
https://doi.org/10.1364/AO.402011
[34] Hameed, A., Parziale, N. J., Paquin, L., Butler, C., and Laurence, S. J., "Spectral Analysis of a Hypersonic Boundary Layer on a Right, Circular Cone," *Proceedings of AIAA SciTech 2020*, AIAA Paper 2020-0362, 2020, pp. 1–14.
https://doi.org/10.2514/6.2020-0362
[35] Harris, A. J., Kreth, P. A., Combs, C. S., and Schmisseur, J. D., "Laser Differential Interferometry and Schlieren as an Approach to Characterizing Freestream Disturbance Levels," *2018 AIAA Aerospace Sciences Meeting*, AIAA Paper 2018-1100, 2018.
https://doi.org/10.2514/6.2018-1100
[36] Lawson, J. M., and Austin, J. M., "Expansion Tube Freestream Disturbance Measurements Using a Focused Laser Differential Interferometer," *Proceedings of AIAA Scitech 2020*, AIAA Paper 2020-1064, 2020.
https://doi.org/10.2514/6.2020-1064
[37] Birch, B., Buttsworth, D., and Zander, F., "Measurements of Freestream Density Fluctuations in a Hypersonic Wind Tunnel," *Experiments in Fluids*, Vol. 61, No. 158, 2020, pp. 1–13.
https://doi.org/10.1007/s00348-020-02992-w
[38] Neet, M., Lawson, J., and Austin, J., "Design, Alignment, and Calibration of a Focused Laser Differential Interferometer," *Applied Optics*, Vol. 60, No. 26, 2021, pp. 7903–7909.
https://doi.org/10.1364/AO.435112
[39] Hedlund, B., Houpt, A., Gordeyev, S., and Leonov, S., "Measurement of Flow Perturbation Spectra in Mach 4.5 Corner Separation Zone," *AIAA Journal*, Vol. 56, No. 7, 2018, pp. 2699–2711.
https://doi.org/10.2514/1.J056576
[40] Houpt, A. W., and Leonov, S. B., "Focused Laser Differential Interferometer for Supersonic Boundary Layer Measurements on Flat Plate Geometries," *Proceedings of the 2018 Plasmadynamics and Lasers Conference*, AIAA Paper 2018-3434, 2018.
https://doi.org/10.2514/6.2018-3434
[41] Houpt, A. W., and Leonov, S. B., "Focused and Cylindrical-Focused Laser Differential Interferometer Characterization of SBR-50 at Mach 2," *Proceedings of AIAA Aviation 2019*, AIAA Paper 2019-3383, 2019.
https://doi.org/10.2514/6.2019-3383
[42] Benitez, E. K., Jewell, J. S., and Schneider, S. P., "Focused Laser Differential Interferometry for Hypersonic Flow Instability Measurements with Contoured Tunnel Windows," *Proceedings of AIAA Scitech 2020*, AIAA Paper 2020-1282, 2020.
https://doi.org/10.2514/6.2020-1282
[43] Benitez, E. K., Esquieu, S., Jewell, J. S., and Schneider, S. P., "Instability Measurements on an Axisymmetric Separation Bubble at Mach 6," *Proceedings of AIAA Aviation 2020*, AIAA Paper 2020-3072, 2020.
https://doi.org/10.2514/6.2020-3072
[44] Benitez, E. K., Jewell, J. S., and Schneider, S. P., "Focused Laser Differential Interferometry with Contoured Tunnel Windows," *AIAA Journal*, Vol. 59, No. 2, 2021, pp. 419–429.
https://doi.org/10.2514/1.J060081
[45] Gragston, M., Siddiqui, F., and Schmisseur, J. D., "Detection of Second-Mode Instabilities on a Flared Cone in Mach 6 Quiet Flow with Linear Array Focused Laser Differential Interferometry," *Experiments in Fluids*, Vol. 62, No. 4, 2021, pp. 1–12.
https://doi.org/10.1007/s00348-021-03188-6
[46] Gragston, M., Price, T. J., Davenport, K., Zhang, Z., and Schmisseur, J. D., "Linear Array Focused-Laser Differential Interferometry for Single-Shot Multi-Point Flow Disturbance Measurements," *Optics Letters*, Vol. 46, No. 1, 2021, pp. 154–157.
https://doi.org/10.1364/OL.412495
[47] Bathel, B., Herring, G. C., Weisberger, J., Chou, A., and Jones, S., "Simultaneous Focused Laser Differential Interferometry and High-Speed Schlieren in a Mach 6 Flow," *Measurement Science and Technology*, Vol. 32, No. 9, 2021, Paper 095907.
https://doi.org/10.1088/1361-6501/abf67a
[48] Fulghum, M. R., "Turbulence Measurements in High-Speed Wind Tunnels Using Focusing Laser Differential Interferometry," Ph.D. Thesis, The Pennsylvania State Univ., State College, PA, 2014.
[49] Settles, G. S., and Fulghum, M. R., "The Focusing Laser Differential Interferometer, an Instrument for Localized Turbulence Measurements in Refractive Flows," *Journal of Fluids Engineering*, Vol. 138, No. 10, 2016, Paper 101402.
https://doi.org/10.1115/1.4033960
[50] Schmidt, B. E., and Shepherd, J. E., "Analysis of Focused Laser Differential Interferometry," *Applied Optics*, Vol. 54, No. 28, 2015, pp. 8459–8472.
https://doi.org/10.1364/AO.54.008459
[51] Ramprakash, A., McIntyre, T. J., Wheatley, V., and Mee, D. J., "Performance Analysis of FLDI Technique Using Turbulent Jets," *Proceedings of the IX Australian Conference on Laser Diagnostics*, Adelaide, Australia, 2019.
[52] Lawson, J. M., Neet, M. C., Grossman, I. J., and Austin, J. M., "Characterization of a Focused Laser Differential Interferometer," *Proceedings of AIAA Scitech 2019*, AIAA Paper 2019-2296, 2019.
https://doi.org/10.2514/6.2019-2296
[53] Lawson, J. M., Neet, M. C., Grossman, I. J., and Austin, J. M., "Static and Dynamic Characterization of a Focused Laser Differential Interferometer," *Experiments in Fluids*, Vol. 61, No. 187, 2020, pp. 1–11.
https://doi.org/10.1007/s00348-020-03013-6
[54] Lawson, J. M., and Austin, J. M., "Focused Laser Differential Interferometer Response to Shock Waves," *Measurement Science and Technology*, Vol. 32, No. 5, 2021, Paper 055203.
https://doi.org/10.1088/1361-6501/abdbd3
[55] Lawson, J. M., "Focused Laser Differential Interferometry," Ph.D. Thesis, California Inst. of Technology, State College, PA, 2021.
https://doi.org/10.7907/5thh-f652
[56] Ceruzzi, A. P., Neisess, C., McManamen, B., and Cadou, C. P., "Investigation of Focused Laser Differential Interferometry (FLDI) Sensitivity Function," *Proceedings of AIAA Scitech 2021*, AIAA Paper 2021-1299, 2021.
https://doi.org/10.2514/6.2021-1299
[57] Pope, S. B., *Turbulent Flows*, 1st ed., Cambridge Univ. Press, Cambridge, England, U.K., 2000, Chap. 6.

M. Borg
Associate Editor